

PAPER • OPEN ACCESS

## Conceptual design of a high temperature superconducting magnet for a particle physics experiment in space

To cite this article: Magnus Dam *et al* 2020 *Supercond. Sci. Technol.* **33** 044012

View the [article online](#) for updates and enhancements.



**IOP | ebooks™**

Bringing together innovative digital publishing with leading authors from the global scientific community.

Start exploring the collection—download the first chapter of every title for free.

# Conceptual design of a high temperature superconducting magnet for a particle physics experiment in space

Magnus Dam<sup>1</sup> , Roberto Battiston<sup>2,3</sup> , William Jerome Burger<sup>3</sup> , Rita Carpentiero<sup>4</sup> , Enrico Chesta<sup>1</sup> , Roberto Iuppa<sup>2,3</sup> , Gijs de Rijk<sup>1</sup>  and Lucio Rossi<sup>1,5</sup> 

<sup>1</sup> CERN, European Organization for Nuclear Research, CH-1211 Geneva 23, Switzerland

<sup>2</sup> Department of Physics, University of Trento, I-38122 Trento TN, Italy

<sup>3</sup> TIFPA, Trento Institute for Fundamental Physics and Applications, I-38123 Povo TN, Italy

<sup>4</sup> ASI, Italian Space Agency, I-00133 Rome RM, Italy

<sup>5</sup> On leave from: Department of Physics, University of Milan, I-20133 Milano MI, Italy

E-mail: [magnus.dam@cern.ch](mailto:magnus.dam@cern.ch)

Received 18 October 2019, revised 28 November 2019

Accepted for publication 31 December 2019

Published 25 February 2020



CrossMark

## Abstract

In the frame of a collaboration between CERN, ASI, University of Trento, and TIFPA, the HTS demonstrator magnet for space project has started to define methods and procedures for manufacturing high temperature superconducting magnets for space applications. To this purpose, we developed a conceptual design of a superconducting magnetic spectrometer for a physics experiment in space. The configuration is a toroid with twelve superconducting coils based on ReBCO tape. By using ReBCO tape with an engineering critical current density,  $J_e$ , exceeding  $1000 \text{ A mm}^{-2}$  at 4.2 K and 20 T, as reached in the H2020-ARIES program, the magnet system provides an average bending strength of 3 T m. This is sufficient to measure charged particles with rigidities up to 100 TV, more than two orders of magnitude higher than the present state-of-the-art space spectrometer. The magnet system requires about 62 km of 12 mm ReBCO tape and produces a peak magnetic field of 11.9 T at an operating temperature of 20 K. A small scale single coil, which is about one third in size of a coil from the toroidal magnet system, will be manufactured and tested as demonstrator of the magnet technology. The mechanical structure and performance of the toroidal magnet system and demonstrator coil are described.

Keywords: space superconducting magnets, HTS superconducting magnets, HTS for space experiments, HTS magnetic spectrometer, HTS toroid, HTS magnet for astroparticle experiment

(Some figures may appear in colour only in the online journal)

## 1. Introduction

Applied superconductivity has great potential for contributing to space missions [1–3], specially particle physics experiments [4–6]. Magnetic spectrometers based on superconducting

magnets can have resolving powers of a factor ten or more above the present state-of-the-art experiment, the Alpha Magnetic Spectrometer (AMS-02) [7], that is running on the International Space Station. A niobium–titanium superconducting magnet cooled by liquid helium was built for AMS-02 [8, 9], but since the limited amount of helium would have resulted in a limited run time of the experiment, it was replaced by a permanent magnet before launch [10].

Since the launch of AMS-02 in 2011, the development in industrial manufacturing methods of high temperature



Original content from this work may be used under the terms of the [Creative Commons Attribution 3.0 licence](https://creativecommons.org/licenses/by/3.0/). Any further distribution of this work must maintain attribution to the author(s) and the title of the work, journal citation and DOI.

superconductor (HTS) wire has made possible building large high field HTS magnets that can operate at higher temperatures to avoid problems related to cooling with liquid helium.

The possibility to extend the sensitivity to particles with rigidities up to a hundred teravolts is driving the design of a future possible particle experiment in space. The European Organization for Nuclear Research (CERN), the Italian Space Agency (ASI), the Department of Physics at the University of Trento, and Trento Institute for Fundamental Physics and Applications are collaborating to develop the concept and technologies for an HTS magnet to be used in a spectrometer for a future space experiment. As working hypothesis, we adopt a 12-coil toroidal magnet system with an outer diameter of 2.0 m and a height of 1.75 m.

The main goal of the HTS demonstrator magnet for space (HDMS) project is to design, manufacture, and test a high-field HTS demonstrator coil based on ReBCO tape suitable for space applications. The coil produced in the HDMS project is interchangeably called the demonstrator coil and the HDMS coil. The coil is about one third in size of a coil from the toroidal magnet system and reaches a peak magnetic field of at least 6.4 T. While the toroidal magnet has an operating temperature of 20 K, the HDMS coil will be tested at 4.2 K to achieve similar performance as a coil from the toroidal magnet system, but it will also be tested at higher temperatures in helium gas.

This paper describes the basic design choices of the toroidal magnet system based on physics requirements and constraints related to space launch, the design of the HDMS coil, as well as the magnetic and structural features of the toroidal magnet and the HDMS coil.

## 2. Constraints for a next generation space spectrometer

This section discusses scientific and technological aspects having impact on the magnet design. Constraints and requirements for the magnet design derive from astrophysical and space engineering considerations.

### 2.1. Physics requirements

A magnetic spectrometer measures the rigidity of a charged particle, defined as  $R = cp/q$  [V], where  $c$  is the speed of light in vacuum,  $p$  is the momentum and  $q$  is the electric charge of the particle. Rigidity is a signed observable, among the few usable to distinguish between matter and antimatter. If an independent estimate of the charge magnitude,  $|q|$ , is available, the momentum of the particle is obtained from the rigidity.

For the simple reference case of a relativistic particle moving in a uniform magnetic field of intensity  $B$ , the following relation holds:  $R = cp_{\perp}/q = \text{sgn}(q)cB\rho$ , where  $p_{\perp}$  is the perpendicular momentum,  $\rho$  is the radius of the circular motion in the plane transverse to the magnetic field, and  $\text{sgn}(\cdot)$  is the sign function. The radius  $\rho$  can be derived from the length of the field region,  $L$ , traversed by the particle and

the sagitta,  $s$ , of the trajectory arc,  $\rho \approx L^2/8s$ . Consequently, the rigidity of the particle is

$$R \approx \text{sgn}(q)c \frac{BL}{8s/L}. \quad (1)$$

If  $B$  and  $L$  are known and  $s$  is measured,  $R$  can be inferred from (1). For sufficiently large rigidity values, it is also possible to infer  $R$  from the angle,  $\theta$ , between the directions of the momentum vectors before,  $\mathbf{p}_i$ , and after,  $\mathbf{p}_f$ , the magnetic field volume

$$R \approx \text{sgn}(q)c \frac{BL}{\theta}, \quad (2)$$

where  $\cos \theta = \mathbf{p}_i \cdot \mathbf{p}_f / (\|\mathbf{p}_i\| \|\mathbf{p}_f\|)$ . If  $BL$  is known and  $\theta$  is measured,  $R$  can be inferred from (2). Equations (1) and (2) show that the particle rigidity can be determined from the ratio of the bending strength,  $BL$ , to the actual bending of the trajectory, quantified as  $8s/L$  or  $\theta$ .

The trajectory of the particle is measured by position-sensitive detectors. Current state-of-the-art silicon detectors employed in space experiments have single hit resolution of about 20  $\mu\text{m}$  and provide track measurements over distances of 1–2 m [11–13]. The corresponding track deflection,  $8s/L \approx \theta \approx 10^{-4}$ , provides the maximum detectable rigidity once the bending strength  $BL$  is set. For instance, AMS-02 [14] with a bending strength of  $BL = 0.13$  T m has according to this estimate  $R_{\text{max}} \approx 1$  TV. The maximum detectable rigidity of AMS-02 is reported to be  $R_{\text{max}} \approx 2$  TV.

A magnetic spectrometer with a maximum detectable rigidity on the order of  $R_{\text{max}} = 100$  TV would represent a significant extension for antimatter studies [15]. The required  $R_{\text{max}}$  could be attained by employing new technologies for particle tracking with single hit resolution down to 4  $\mu\text{m}$  [16, 17], compatible with space application requirements [18]. With a lever arm of 1 m, a bending strength of 1 T m would be sufficient, whereas a  $BL$  of 3 T m would allow the spectrometer to be sensitive to cosmic antimatter up to 100 TV within just 30 cm.

### 2.2. Acceptance

The cosmic-ray rigidity spectra follow a steep power law  $kR^{-\alpha}$ , with  $\alpha$  ranging from 2 to 4, depending on the particle species [19]. A significantly larger acceptance is needed to maintain sensitivity at a factor 100 higher rigidity than the current state-of-the-art AMS-02 experiment, with an acceptance about 500  $\text{cm}^2$  sr at  $R_{\text{max}} = 2$  TV. Detection acceptances of the order of 1–10  $\text{m}^2$  sr are needed to attain the required sensitivity at about 100 TV. Sensitive areas of a few square meters are impossible to obtain with single-sided spectrometers like AMS-02, employing a dipolar magnetic field, because the instrumented volume would readily exceed the fairing volume of available launchers. A toroidal geometry is preferable since the measurements may be made over a significantly wider angular acceptance, essentially for all arrival directions of the incident particles passing through the spectrometer.

### 2.3. Space engineering requirements

Equation (1) shows that rigidity increases with  $L^2$ , while it only increases linearly with  $B$ . Hence, a high rigidity is more easily obtained with a large magnetic volume than with a high magnetic field. For this reason, particle detectors, like the ATLAS experiment [20] and the Compact Muon Solenoid [21] at the Large Hadron Collider at CERN, usually feature huge volumes and medium magnetic fields of 2–4 T. However, volume and weight are highly constrained for space launch, making a high magnetic field a key ingredient to high resolution regimes.

To be launched to orbit, the experiment must be compatible with the fairing volume and payload mass limit of the launcher [22, 23]. The choice of the launcher is determined by the orbit required for the experiment. We aim to keep the outer diameter of the entire experiment below 3 m and the total mass below 6000 kg.

The magnet system is required to have a vanishing total magnetic moment to avoid coupling with external magnetic fields such as the Earth’s magnetic field or the interplanetary magnetic field, depending on the experiment location. This would cause rotation or drifting of the hosting satellite. A toroidal magnet configuration has the advantage to naturally fulfill this requirement. Small coil displacement errors cause a nonzero total magnetic moment, that can be canceled out with magnetorquers [24].

The cooling of the magnet should be cryogen-free [25] to avoid that a limited amount of cryogen restricts the lifetime of the experiment. The magnet should operate within the temperature range from 10 to 20 K to maximize the refrigeration efficiency to cope with the limited electric power available in space. This also has the benefit of making the operation of the magnet less sensitive to small temperature variations. At these temperatures it should be possible to run the experiment as long as the power source is available and the functioning of the cryocoolers can be assured.

Designing and building payloads with the highest reliability is strictly required in the field of space engineering [26]. A superconducting magnet requires special attention, considering the large amount of energy stored in the magnetic field and the need to reliably operate at cryogenic temperatures. The design must ensure that the superconducting magnet can withstand the challenges of launch, deployment and operation in space. A failure of a superconducting magnet subsystem during operation should minimally affect the overall payload.

The demonstrator coil is a first step toward space qualification. The demonstrator coil must avoid reliance on technologies known to be problematic for successfully passing the tests required for space qualification, even if these tests are not foreseen to be carried out on the demonstrator.

### 2.4. Reference layout

The baseline design for a magnetic spectrometer for space which responds to the aforementioned requirements and constraints was implemented in the Geant4 Monte Carlo

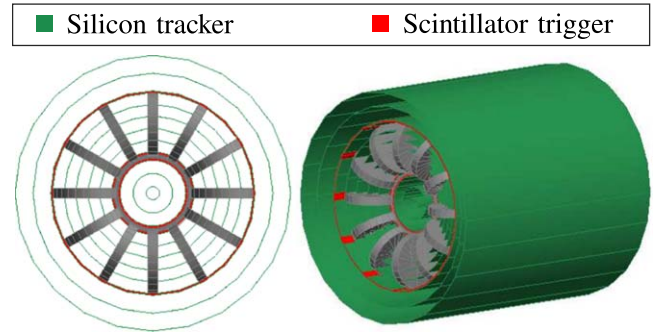


**Figure 1.** The geometric description of the HTS magnetic spectrometer in the Geant4 simulation. The magnet coils and support cylinder are shown in gray. The locations of the outer, middle and inner silicon tracker layers (green) and scintillator trigger layers (red) are sketched.

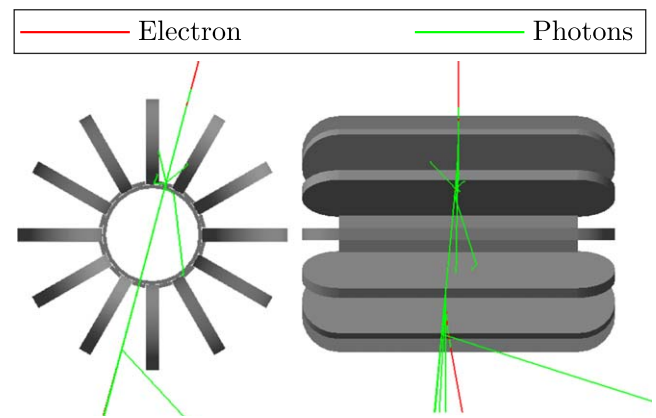


**Figure 2.** The trajectory of an electron with a rigidity of 10 GV. The electron passes all the way through the toroidal magnet and is deflected in opposite directions in the two opposing field regions of the magnet. The electron trajectory is partly hidden by the overlapping photons trajectories.

simulation program [27] to evaluate the performance of the detector. The geometry of the HTS magnetic spectrometer in the simulation is shown in figure 1. The average bending strength of the twelve coil configuration is  $BL = 3 \text{ T m}$ . The inner and outer diameters of the toroid are 50 cm and 200 cm, respectively. Silicon-based detector layers (green) provide track measurements throughout the toroidal field volume, at the entry and exit of the toroid, and in the field-free volume in the center of the toroid. Trigger detectors (red) delimit the three regions providing the time-ordered coincidences used to identify the presence, and define the direction of the passing particles. The field-free volume inside the toroid may be used to host a calorimeter if required for particle identification.

Figures 2 and 3 show the trajectories of an electron and a proton, respectively, both with a rigidity of  $R = 10 \text{ GV}$ . The mechanical structure is shown, while the detector layers are hidden. In the figures, the electron and proton enter the magnetic field from the top. The particles only deflect in the direction of the toroidal axis, and the rigidity can be determined from this deflection. The magnetic force,  $F = qv \times B$ ,

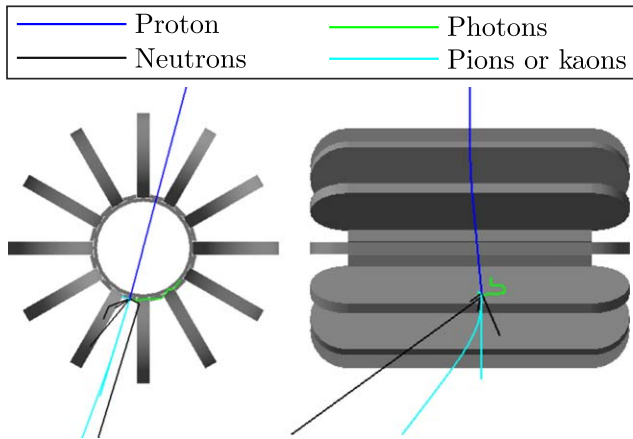


**Figure 3.** The trajectory of a proton with a rigidity of 10 GV in the toroidal magnetic field. The proton deflects along the direction of the toroidal axis and collides with the mechanical structure after passing through the field-free region.

deflects the electron and proton in opposite directions due to their opposite charges.

Figure 2 illustrates the deflection of the electron in the magnetic field. The electron passes all the way through the magnet and deflects in opposite directions in the two opposing magnetic field regions. The electron is accompanied by collinear synchrotron radiation photons (green) which continue along the original direction of the electron.

Figure 3 illustrates the deflection of the proton in the magnetic field. The proton traverses the magnetic field and the central field-free region, but is stopped by an inelastic nuclear interaction in the aluminum inner intercoil structure. The other visible trajectories represent secondary neutrons (black), photons (green), and pions or kaons (cyan).

### 3. Conceptual design of the toroidal magnet system

This section describes the design of a toroidal magnet system for a magnetic spectrometer for a space experiment. The magnet design fulfills all the physics requirements and constraints related to space launch outlined in section 2.

#### 3.1. Conductor requirements and winding method

The coils are designed to be built with 12 mm wide HTS ReBCO tape. ReBCO tape has been tested in short lengths to have an engineering critical current density exceeding  $J_e = 1000 \text{ A mm}^{-2}$  at 4.2 K in a 20 T magnetic field [28]. Within the next few years, we anticipate HTS tape with a performance of  $J_{e,0} = J_e(4.2 \text{ K}, 20 \text{ T}) = 1200 \text{ A mm}^{-2}$  to be available in long lengths from HTS wire manufacturers, and we assume that such tape can be used for building the coils of the toroidal magnet system.

To convert the value of the engineering critical current density given at 4.2 K and 20 T into corresponding values at other temperatures and magnetic field strengths, we used a fitting function [29]. Figure 4 shows the magnetic field and temperature dependence of the critical current density given

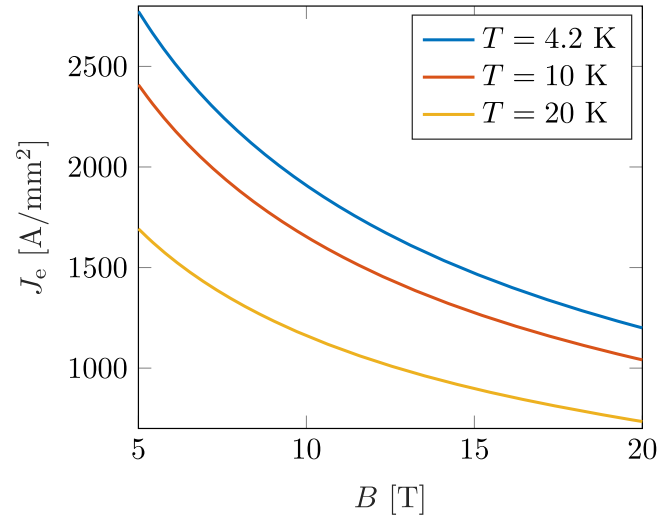


**Figure 4.** The engineering critical current density,  $J_e$ , as a function of the magnetic field strength at different temperatures if  $J_e = 1200 \text{ A mm}^{-2}$  at 4.2 K in a 20 T magnetic field. This  $J_e$  is assumed for the HTS tape used for the coils of the toroid.

by the fitting function with parameters derived from a characterization of one specific type of HTS tape and scaled to obtain  $J_{e,0} = 1200 \text{ A mm}^{-2}$ . The critical current density also depends on the angle between the magnetic field and the tape surface, but this dependence is neglected and the conductor requirements are for worst case conditions when the magnetic field is parallel to the  $c$ -axis of the HTS layer. We assume a tape thickness of  $100 \mu\text{m}$ , which includes  $2 \times 20 \mu\text{m}$  of copper surround stabilizer.

If the cable were insulated and we were to require the peak temperature to stay below 200 K, while the magnet discharges over a dump resistor after the detection of a quench, the voltage drop over the dump resistor would be tens of kilovolts. This is due to the small quantity of stabilizing copper in presence of a very high engineering operating current density. Hence, instead we plan to build the coils with metal-insulated cable [30–32] to allow current sharing between winding turns. Detection of a quench activates a breaker that opens the coil circuit of each individual coil pack to let the coils slowly discharge internally through the turn-to-turn resistance. The generated heat becomes evenly distributed over the entire coil system. We expect that a system based on this self-protection concept provides sufficient quench protection for the magnet.

Figure 5 shows a sketch of the winding scheme. The cable consists of two stacked HTS tapes with the internal ReBCO layers in face-to-face configuration and a coated steel tape to provide partial insulation between turns. The alloy composition and coating type of the metal insulation tape determines the resistance between turns. The turn-to-turn resistance should be sufficiently high that the current stays in the cable during normal operation, and sufficiently low that the voltage drop over each coil stays below 1 kV during a quench. Each tape is solder coated with a low melting temperature solder alloy. After winding the coil, the entire coil is heated above the solder melting point and cooled again.

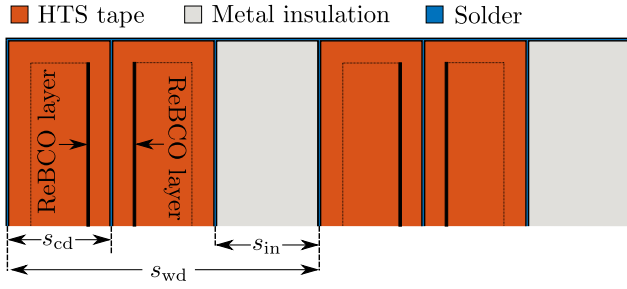


**Figure 5.** Sketch of a cross section of the winding scheme showing the top part of two winding turns. The cable consists of two stacked HTS tapes in face-to-face configuration and one metal tape. Solder fills the small gaps between tapes in the cable and between winding turns.

**Table 1.** Provisional parameters for the conductor cable consisting of two HTS tapes and one metal insulation tape.

Symbol	Description	Value	Unit
$J_{e,0}$	$J_c$ (4.2 K, 20 T)	1200	$A\ mm^{-2}$
$s_{cd}$	HTS tape thickness	100	$\mu m$
$s_{in}$	Metal insulation thickness	100	$\mu m$
$n_{cd}$	HTS tapes per cable	2	—
$s_{wd}$	Cable thickness	300	$\mu m$
$w_{wd}$	Tape and cable width	12	mm
$\rho_{wd}$	Cable mass density	8270	$kg\ m^{-3}$

This procedure avoids depositing a thick layer of solder on the top and bottom of the winding layer. The solder ensures good electrical connections with controlled resistance between turns. Table 1 specifies the main parameters for the HTS tape and cable.

A metal insulated coil has a larger charging loss than a normally insulated coil. To keep the heat generation during charging below the cooling capacity of the cryocoolers, the coils can be charged slowly over a long period of time. The concept of metal-insulation between turns has to be comprehensively investigated to confirm that it is a suitable choice for the coils of the toroidal magnet system. A winding machine capable of simultaneously winding multiple tapes onto a single coil with controlled winding tension is under assembly in our laboratory. We will first test metal-insulation and the winding procedure in a series of small solenoid test coils, and then with the racetrack demonstrator coil. With the demonstrator coil, we will also investigate possible technical challenges related to screening current effects and quench protection.

### 3.2. Coil design

The bending strength is the magnetic field component perpendicular to the particle velocity integrated along the particle trajectory. The bending strength depends on the particle trajectory and should in principle be computed statistically by averaging over the bending strengths of a large number of particle trajectories. To be able to make quick design comparisons, we estimate the bending strength by only

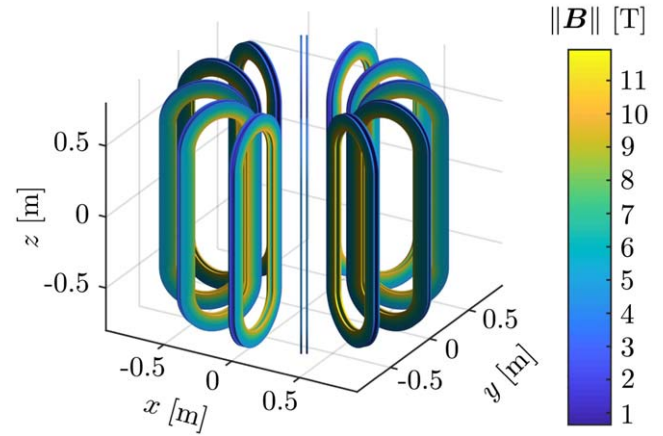


**Figure 6.** Magnetic field strength on the conductor surfaces of the toroidal magnet system.

considering particles moving in straight lines through the origin in the cross sectional central plane of the toroid. We decompose the magnetic field into its polar components  $B_r$  and  $B_\varphi$ , whereof only  $B_\varphi$  contributes to the bending. For each fixed angle  $\varphi \in [0, \pi/N]$ , where  $N = 12$  is the number of coils, we average  $B_\varphi$  over a range of length  $L = r_{tor}$  ending at the origin

$$\bar{B}_\varphi(\varphi) = \frac{1}{L} \int_0^L B_\varphi(r, \varphi) dr. \quad (3)$$

Hence, the bending strength averaged over the toroidal angle  $\varphi$  is

$$\langle \bar{B}_\varphi L \rangle = \frac{N}{\pi} \int_0^{\pi/N} \bar{B}_\varphi(\varphi) L d\varphi. \quad (4)$$

The design of the toroidal magnet system focuses on fulfilling the requirement of an average bending strength of  $\langle \bar{B}_\varphi L \rangle = 3\ Tm$  under the given constraints.

The number of coils in the toroid is chosen as a trade-off between conflicting requirements: best field uniformity and maximum volume free of mechanical structure. Eventually, we selected a configuration with twelve coils. In a configuration with fewer coils, the peak field would be significantly higher, and the stronger Lorentz forces would necessitate much more mechanical structure around each coil. A different requirement on the bending strength or different constraints on the toroid could have resulted in a different choice for the number of coils. For instance, a toroid with an outer diameter of at least 2.4 m, the same inner diameter, and same bending strength requirement, would need a lower average magnetic field, making a configuration with eight coils a better choice, a solution adopted for other large toroidal configurations, like ATLAS.

The straight segment height of the coils is 1 m. Each coil is racetrack shaped, since this shape very well approximates the coil shape that minimizes bending stresses in these narrow coils [33]. The magnet operates at a temperature of 20 K to facilitate cryogen-free cooling.

Figure 6 shows the toroidal coil configuration and the magnetic field strength on the conductor surfaces. Each of the

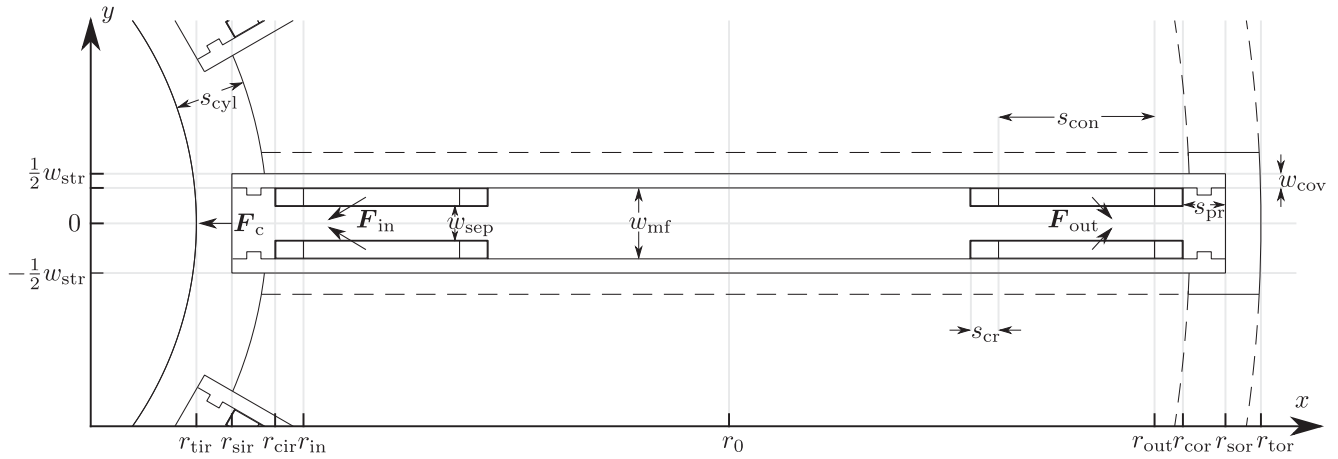


**Figure 7.** Cross sectional sketch of one coil pack from the toroidal magnet system. The characterizing geometrical parameters of the mechanical structure are shown together with the forces.

twelve coils contains two winding layers. About 62 km of 12 mm HTS tape is needed for the entire magnet system. The engineering operating current density in the HTS tape is  $J_{op} = 855 \text{ A mm}^{-2}$  at 20 K with a peak magnetic field of 11.9 T. The main design parameters of the coils are listed in table 2.

We build each coil layer by winding the cable around an elongated copper band and enclosing the winding layer with a larger elongated copper band. The copper bands serve the purpose of transferring the current in and out of the tape with a low contact resistance of about 10 n $\Omega$ . We plan to test this concept before building the coils.

Building the coils with metal insulated soldered cable should make the coil system self-protected. Assume all the magnetic energy is converted into heat distributed uniformly over the coil material. This increases the specific enthalpy of the coil material by  $\Delta h_p = E_m / m_{coil} = 30.5 \text{ kJ kg}^{-1}$ . Assuming the specific enthalpy of the coil material is the same as for copper, the temperature of the coil material increases from  $T_{op} = 20 \text{ K}$  to  $T_f \approx 166 \text{ K}$ . Hence, if the magnetic energy is distributed sufficiently fast over the coil material after the occurrence of a quench, the magnet remains undamaged.

### 3.3. Forces and mechanical structure

The mechanical structure will be made from Aluminum 2050-T84 alloy to minimize the mass of the magnet system. With a yield strength of about 462 MPa at room temperature [34], this aluminum alloy is sufficiently strong to withstand the Lorentz forces produced by the coils. Thermal contraction of the mechanical structure adds a pre-stress to the coil, which reduces the radial coil stresses in operation mode.

Figure 7 shows a cross section of the coil and the mechanical structure. The Lorentz force on each half winding layer and the total Lorentz force on the coil pack are marked with arrows. Here,  $F_{in}$  is the force acting on the part of the winding layer for which  $r < r_0$ ,  $F_{out}$  is the force acting on the part of the winding layer for which  $r > r_0$ , and

**Table 2.** Provisional design parameters for the coils of the toroidal magnet system.

Symbol	Description	Value	Unit
$z_0$	Half straight conductor height	500.0	mm
$z_{out}$	Half max. conductor height	800.0	mm
$r_0$	Central radial coil location	625.0	mm
$r_{in}$	Inner radius for conductor	325.0	mm
$r_{out}$	Outer radius for conductor	925.0	mm
$r_{cir}$	Inner radius for coil	305.0	mm
$r_{cor}$	Outer radius for coil	945.0	mm
$d_{out}$	Conductor outer diameter	600.0	mm
$s_{con}$	Conductor thickness	110.0	mm
$w_{sep}$	Layer separation width	25.0	mm
$s_{cb}$	Thickness of copper bands	19.5	mm
$s_{ins}$	Insulation thickness	0.5	mm
$L_{wd}$	Conductor cable length	31	km
$L_{sc}$	HTS tape length	62	km
$m_{wd}$	Conductor cable mass	927	kg
$m_{coil}$	Coil mass	1298	kg
$T_{op}$	Operating temperature	20	K
$B_{peak}$	Peak magnetic field	11.9	T
$J_{op}$	Eng. operating current density	855	A mm <sup>-2</sup>
$J_e$	Critical eng. current density	1042	A mm <sup>-2</sup>
$I_{op}$	Cable operating current	2052	A
$E_m$	Stored energy	39.6	MJ
$L_m$	Inductance	18.8	H

$F_c = F_{in} + F_{out}$ . The magnitudes of the forces  $F_{in}$  and  $F_{out}$  are identical for the two layers, so the same symbol applies to either layer.

Table 3 lists the components of the Lorentz forces on the half part of the winding layer near the inside of the toroid,  $F_{in} = (F_{in,x}, F_{in,y}, F_{in,z})^T$ , the components of the Lorentz force on the winding layer part near the outside of the toroid,  $F_{out} = (F_{out,x}, F_{out,y}, F_{out,z})^T$ , and the magnitude of the net force acting of the coil pack,  $F_c = \|F_c\|$ , directed toward the toroid center. Table 4 lists the geometrical parameters for the mechanical structure.

Figure 8 shows the coil layers being inserted into the mechanical structure. The current enters into one coil layer

**Table 3.** The Lorentz forces acting on half a winding layer of the toroidal magnet system.

Symbol	Description	Value	Unit
$F_{in,x}$	Lorentz force $x$ -component (in)	-4.7	MN
$F_{in,y}$	Lorentz force $y$ -component (in)	$\pm 2.8$	MN
$F_{in,z}$	Lorentz force $z$ -component (in)	0.0	MN
$F_{out,x}$	Lorentz force $x$ -component (out)	2.7	MN
$F_{out,y}$	Lorentz force $y$ -component (out)	$\pm 2.9$	MN
$F_{out,z}$	Lorentz force $z$ -component (out)	0.0	MN
$F_c$	Net force on coil pack	4.0	MN

**Table 4.** Provisional main parameters for the mechanical structure of the toroidal magnet system.

Symbol	Description	Value	Unit
$r_{tir}$	Toroid inner radius	250	mm
$r_{tor}$	Toroid outer radius	1000	mm
$r_{sir}$	Structure inner radius	275	mm
$r_{sor}$	Structure outer radius	975	mm
$z_{str}$	Half structure height	850	mm
$z_t$	Half toroid height	875	mm
$d_{str}$	Structure outer diameter	700	mm
$s_{pr}$	Protrusion thickness	30	mm
$w_{cov}$	Cover plate width	10	mm
$w_{mf}$	Magnet former width	50	mm
$w_{str}$	Structure width	70	mm
$s_{cyl}$	Cylinder thickness	50	mm
$m_{cps}$	Coil pack structure mass	2243	kg
$m_{cp}$	Coil pack mass	3541	kg
$m_{ics}$	Intercoil structure mass	1036	kg
$m_t$	Total toroid mass	4577	kg
$\sigma_{str}$	Maximum stress in structure	383	MPa
$\sigma_{con}$	Maximum stress in conductor	370	MPa

and leaves from the second layer. The racetrack shapes of the coil layers are machined into each side of a 50 mm aluminum alloy plate which functions as a magnet former. The coil layers are inserted into the former. The layers are electrically connected with braided copper connectors through a hole in the magnet former. The coil layers are enclosed by 10 mm cover plates bolted to the magnet former, which makes the total thickness of the coil pack structure 70 mm.

Figure 9 shows the von Mises stress on the surface of the mechanical structure and coils computed with ANSYS<sup>®</sup> Mechanical, Release 2019 R1. To model coil layers directly inserted into the former, we defined frictionless contacts between the coil insulation and the mechanical structure. A maximum stress of about 383 MPa is observed on the magnet former in the corner that the coil layer presses against. The maximum stress is below the yield strength of the aluminum alloy, which is sufficient for this preliminary design. The maximum von Mises stress on the conductor is 370 MPa, caused by a slight bending of the winding layers toward each other. We expect no degradation of the superconducting tape for stresses below 500 MPa [35], so this value is acceptable.

**Table 5.** Nominal performance parameters for the toroidal magnet.

Symbol	Description	Value	Unit
$B_{xy}$	Maximum $B$ -field in $xy$ -plane	11.4	T
$B_0$	Maximum $B$ -field at $r = r_0$	5.9	T
$B_{tir}$	Maximum $B$ -field at $r = r_{tir}$	0.1	T
$B_{tor}$	Maximum $B$ -field at $r = r_{tor}$	0.9	T
$\min_{\varphi} \bar{B}_{\varphi} L$	Minimum bending strength	2.94	T m
$\max_{\varphi} \bar{B}_{\varphi} L$	Maximum bending strength	3.06	T m
$\langle \bar{B}_{\varphi} L \rangle$	Average bending strength	3.00	T m

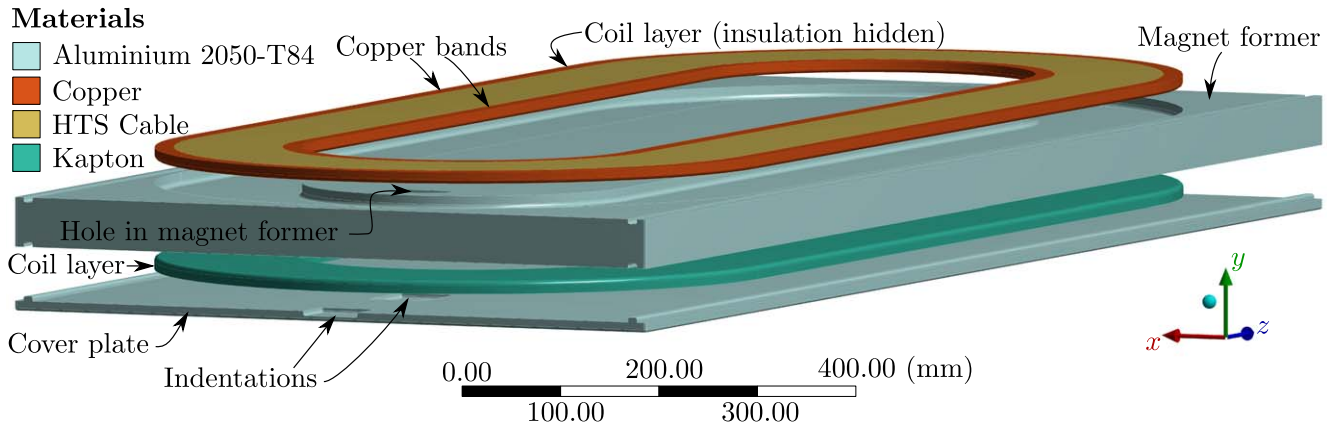
The actual forces will be lower, since there is in reality some friction between the insulation and mechanical structure that will transfer some stress to the former. The stress causes a deformation that opens up a 0.3 mm wide gap between the inside of the racetrack shaped coil layer and the magnet former.

Figure 10 shows the entire mechanical structure of the toroidal magnet system. The sum of Lorentz forces on each coil pack is directed toward the toroid center. A 25 mm thick aluminum alloy cylinder constitutes the inner intercoil structure. An outer intercoil structure is added to stabilize the toroid against small perturbations and large symmetry breakdowns of the forces acting on the coil system. The outer intercoil structure consists of three connected cylindrical bands wrapped around the toroid. Structural mechanical connections between the inner and outer intercoil structure are located at the top and bottom of each coil pack to prevent rotational displacements.

The spectrometer magnet requires specially designed cryocoolers to keep the magnet at its operating temperature of 20 K. We plan to cool down the entire mechanical structure together with the coils, which gives a cold mass of about 4600 kg. The mass of the mechanical structure could potentially be reduced by topology optimization [36] of the mechanical structure.

### 3.4. Field characterization

Figure 11 shows the magnetic field in the cross sectional central plane of the toroid, where the maximum magnetic field is 11.4 T. Figure 12 shows the bending strength of the toroidal magnet as a function of the toroidal angle,  $\varphi$ , for a particle moving in the central plane of the toroid from outside the toroid to the center as defined by (3). The bending strength varies periodically as a function of the toroidal angle. The bending strength is 2.94 T m for trajectories equally distant to two neighboring coil packs, and it is 3.06 T m for trajectories through the middle of a coil pack. By design, the average bending strength (4) is  $\langle \bar{B}_{\varphi} L \rangle = 3$  T m. For particles that pass through the center and continue through the opposing magnetic field, the bending strength would be twice this value. Table 5 lists performance parameters for the magnet system.



**Figure 8.** The mechanical structure of one coil pack of the toroidal magnet system. The insulation and cover plate are hidden for the upper part. The shapes of the coil layers are machined into the magnet former. Cover plates hold the coil layers in place. The two coil layers are electrically connected with a braided copper connector going through a hole in the magnet former. The current inlet and outlet are connected through indentations in the cover plate.

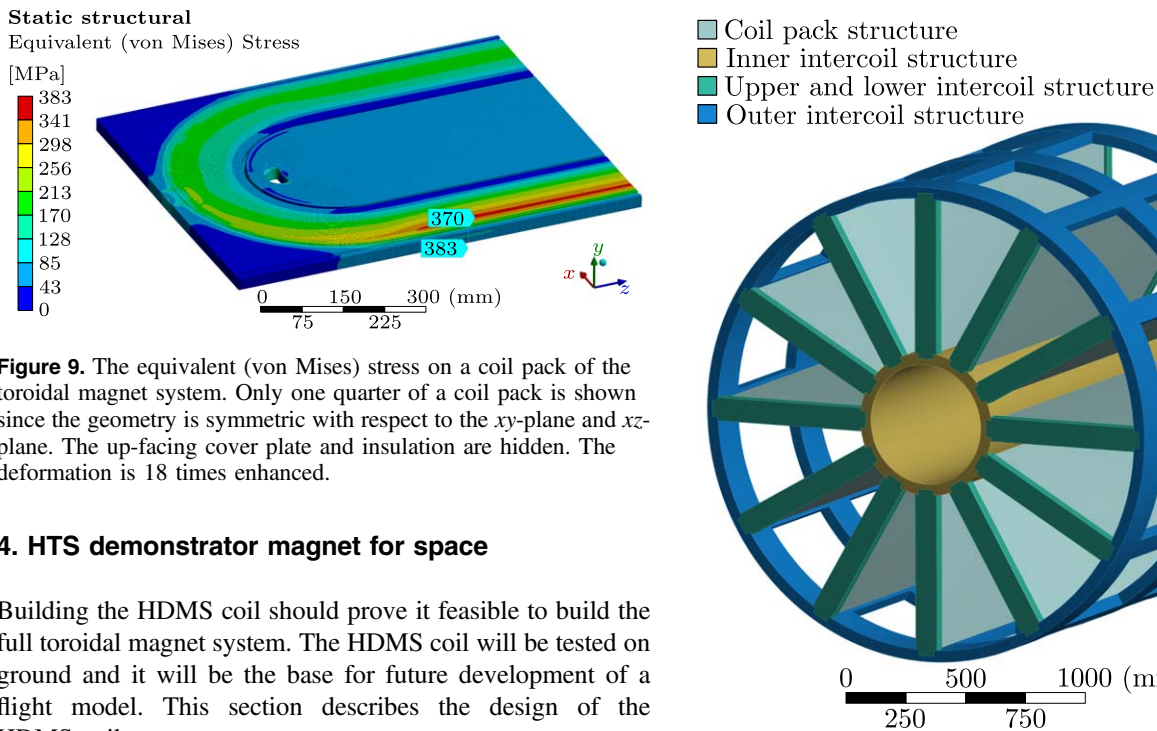


**Figure 9.** The equivalent (von Mises) stress on a coil pack of the toroidal magnet system. Only one quarter of a coil pack is shown since the geometry is symmetric with respect to the  $xy$ -plane and  $xz$ -plane. The up-facing cover plate and insulation are hidden. The deformation is 18 times enhanced.

#### 4. HTS demonstrator magnet for space

Building the HDMS coil should prove it feasible to build the full toroidal magnet system. The HDMS coil will be tested on ground and it will be the base for future development of a flight model. This section describes the design of the HDMS coil.

##### 4.1. Conductor specification

For building the HDMS coil, we will have about 1 km of 12 mm ReBCO HTS tape available with an engineering critical current density of at least  $J_e = 400 \text{ A mm}^{-2}$  at 4.2 K and in a 20 T magnetic field. Figure 13 shows the engineering critical current density dependency on the magnetic field and temperature. To achieve a sufficiently high magnetic field with this tape, that is much lower performing than the tape specified for the toroidal magnet, we set the operating temperature for the HDMS coil to 4.2 K instead of 20 K. However, we design the demonstrator with the same dry coil concept as the space experiment, and we will also test the demonstrator at variable temperatures to test the thermal design. The same cable configuration and winding method

**Figure 10.** The intercoil structure made from Aluminum 2050-T84 keeps the coils in fixed locations. The inner intercoil structure is an inner cylinder that absorbs the force from each coil pack directed toward the toroid center. The outer intercoil structure consists of three connected cylindrical bands and keeps the coils in their mechanically unstable equilibriums. The upper and lower intercoil structure are supporting connections between the inner and outer intercoil structure to avoid rotational displacements.

will be used for building the HDMS coil as described in section 3.1 for the toroidal magnet coils.

##### 4.2. Coil design

The HDMS design is a smaller version of one coil pack of the toroidal magnet system. The straight parts of the HDMS

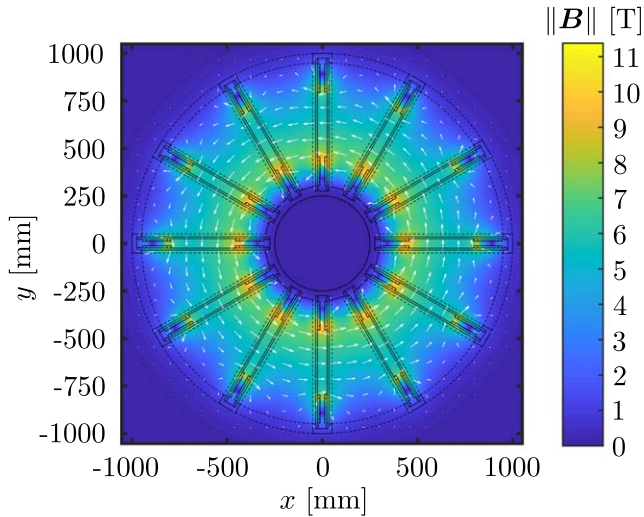


**Figure 11.** The boundaries of the coils and mechanical structure of the toroidal magnet system sketched on top of the magnetic field strength in the  $xy$ -plane.

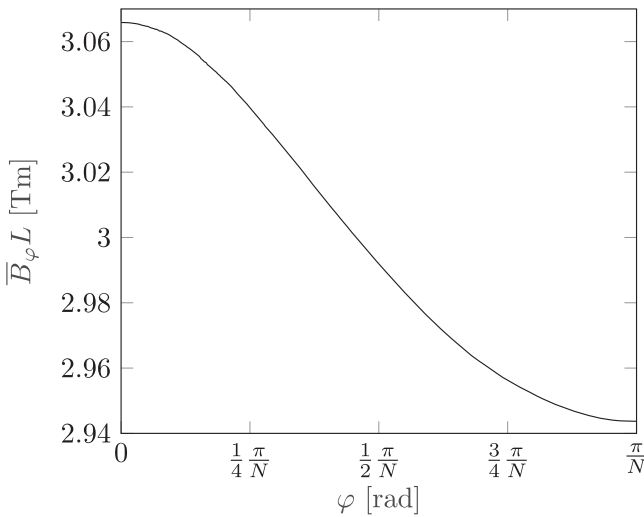
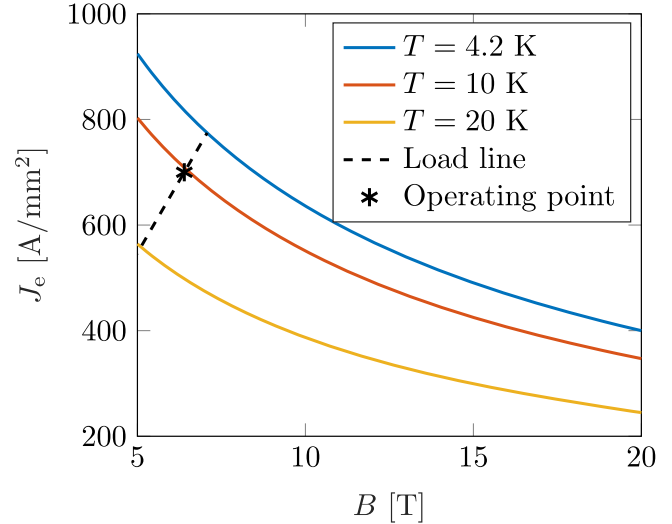


**Figure 12.** The bending strength as a function of toroidal angle in a single detector sector of the toroid.  $N = 12$  is the number of coils.

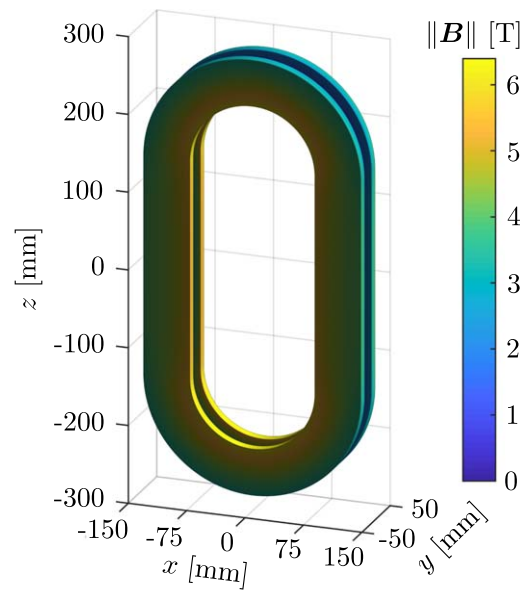
racetrack shapes are 280 mm, i.e. almost one third of the straight parts of a toroid coil. This makes the demonstrator coil very significant, also for testing the construction procedure.

Figure 14 shows the magnetic field on the surface of the two winding layers of the HDMS coil. The operating current density is  $J_{op} = 700 \text{ A mm}^{-2}$  at 4.2 K with a peak magnetic field of 6.4 T. Like the coils of the toroidal magnet, the current will be transferred in and out of the HTS cable through elongated copper bands located on the inside and on the outside of the winding layers. Table 6 lists the main design parameters of the coils.

The HDMS coil is designed to be self-protected. A conversion of the magnetic energy into heat distributed uniformly over the HDMS coil material increases the specific enthalpy of the coil material by  $\Delta h_p = E_m / m_{coil} = 4.1 \text{ kJ kg}^{-1}$ . Assuming the specific enthalpy of the coil material is the same as for



**Figure 13.** The engineering critical current density,  $J_e$ , as a function of the magnetic field strength at different temperatures if  $J_e = 400 \text{ A mm}^{-2}$  at 4.2 K in a 20 T magnetic field. This  $J_e$  is assumed as a minimum requirement for the HTS tape used for the demonstrator coil.



**Figure 14.** The magnetic field strength on the conductor surfaces of the demonstrator coil operating at  $J_{op} = 700 \text{ A mm}^{-2}$  at 4.2 K.

copper, the temperature of the coil material increases from  $T_{op} = 4.2 \text{ K}$  to  $T_f \approx 70 \text{ K}$ .

#### 4.3. Forces and mechanical structure

The mechanical structure of the HDMS coil will be made from Aluminum 2050-T84 like planned for the toroid structure. Figure 15 shows a cross section of the HDMS coil and the mechanical structure. The directions of the Lorentz force,  $F_L$ , on each half winding layer, split through  $x = 0$ , are marked with arrows. The entire geometry is symmetric with respect to the  $xz$ -plane and the  $yz$ -plane. Hence, the net force on the coil

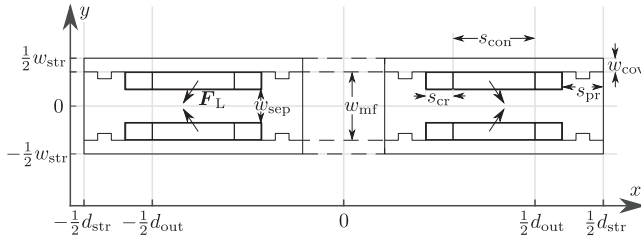


**Figure 15.** Cross sectional sketch of the demonstrator coil. The characterizing geometrical parameters of the mechanical structure are shown together with the forces.

**Table 6.** Provisional design parameters for the demonstrator coil.

Symbol	Description	Value	Unit
$z_0$	Half straight conductor height	140.0	mm
$z_{out}$	Half max. conductor height	280.0	mm
$d_{out}$	Conductor outer diameter	280.0	mm
$s_{con}$	Conductor thickness	60.0	mm
$w_{sep}$	Layer separation width	25.0	mm
$s_{cb}$	Thickness of copper bands	19.5	mm
$s_{ins}$	Insulation thickness	0.5	mm
$L_{wd}$	Conductor cable length	0.5	km
$L_{sc}$	HTS tape length	1.0	km
$m_{wd}$	Conductor cable mass	14.9	kg
$m_{coil}$	Coil mass	25.6	kg
$T_{op}$	Operating temperature	4.2	K
$B_{peak}$	Peak magnetic field	6.4	T
$J_{op}$	Eng. operating current density	700	A mm <sup>-2</sup>
$J_e$	Critical eng. current density	817	A mm <sup>-2</sup>
$I_{op}$	Cable operating current	1680	A
$E_m$	Stored energy	106	kJ
$L_m$	Inductance	75.1	mH

**Table 7.** The Lorentz force on half a winding layer of the demonstrator coil.

Symbol	Description	Value	Unit
$F_x$	Lorentz force $x$ -component	$\pm 181$	kN
$F_y$	Lorentz force $y$ -component	$\pm 272$	kN
$F_z$	Lorentz force $z$ -component	0	kN
$F_L$	Lorentz force magnitude	327	kN

pack is zero. The values of the Lorentz force components are listed in table 7. Here,  $\mathbf{F}_L = (F_x, F_y, F_z)^T$  denotes the force on either of the four half winding layers, while  $F_L = \|\mathbf{F}_L\|$  is the force magnitude. Table 8 lists the main design parameters for the mechanical structure of the HDMS coil.

Figure 16 shows the mechanical structure of the HDMS coil. The coil structure resembles the one designed for the toroidal magnet coils with some unnecessary structure material removed. The current inlet and outlet are through indentations in the bottom part of the cover plates, and the coil layers are connected through the elongated central hole in the magnet former.

Figure 17 shows the von Mises stress on the surface of the coil and mechanical structure. With the lower magnetic

**Table 8.** Provisional design parameters for the mechanical structure of the demonstrator coil.

Symbol	Description	Value	Unit
$z_{str}$	Half structure height	330	mm
$d_{str}$	Structure outer diameter	380	mm
$s_{pr}$	Protrusion thickness	30	mm
$w_{cov}$	Cover plate width	10	mm
$w_{mf}$	Magnet former width	50	mm
$w_{str}$	Structure width	70	mm
$m_{str}$	Structure mass	29	kg
$m_{cp}$	HDMS coil pack mass	55	kg
$\sigma_{str}$	Maximum stress in structure	233	MPa
$\sigma_{con}$	Maximum stress in conductor	111	MPa

field, the stress in the mechanical structure of the HDMS coil is lower than in the structure of a coil pack for the toroid. The maximum von Mises stress in the magnet former is about 233 MPa and in the conductor it is about 111 MPa. The stress causes a deformation that opens up a 0.06 mm wide gap between the coil and the magnet former.

#### 4.4. Performance

Figure 18 shows the magnetic field in the cross sectional central plane of the HDMS coil, where the maximum magnetic field is 5.5 T. The location of the boundaries of the coil and mechanical structure are shown. The field in the center of the coil is 2.7 T.

To define the bending strength of a single coil, we decompose the magnetic field into its Cartesian components  $B_x$  and  $B_y$ , whereof only  $B_y$  contributes to the bending. For each fixed value of  $y$ , we average  $B_y$  over  $x \in [-d_{out}/2, d_{out}/2]$

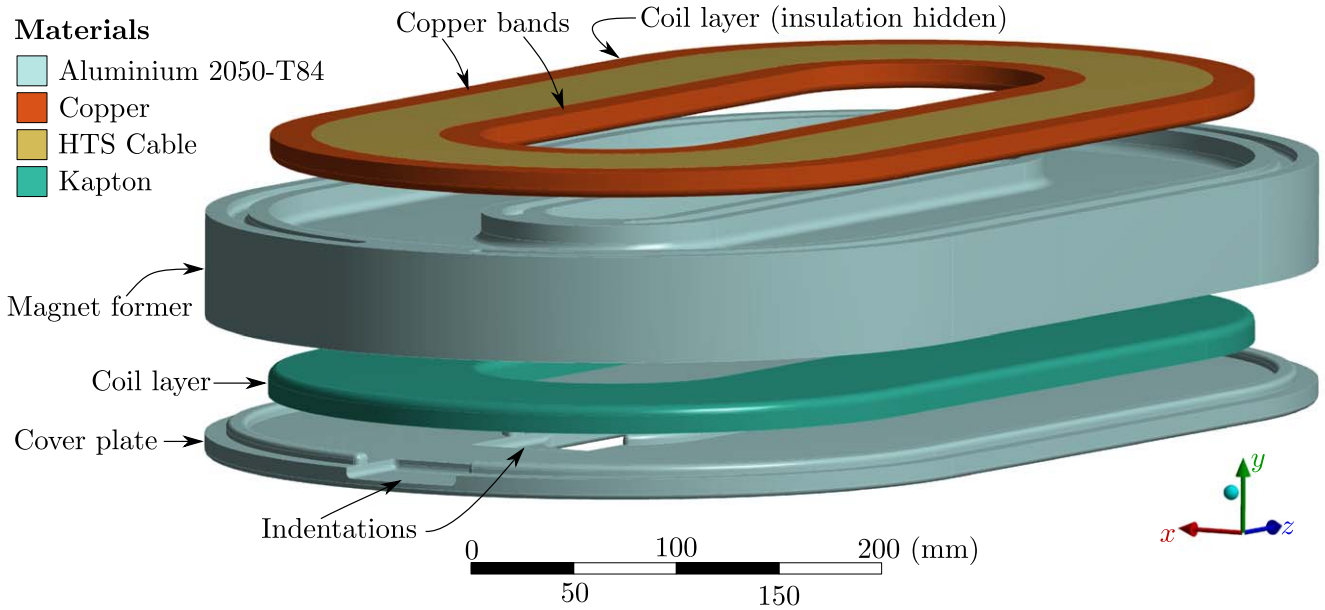
$$\bar{B}_y(y) = \frac{1}{L} \int_{-d_{out}/2}^{d_{out}/2} B_y(x, y) dx, \quad L = d_{out}. \quad (5)$$

Figure 19 shows the bending strength (5) of the HDMS coil as a function of the distance from the coil center for particle trajectories parallel to the  $x$ -axis of figure 18. The regions respectively occupied by mechanical structure and conductor are sketched. The maximum bending strength of the HDMS coil outside the cover plate is about 0.5 T m, which is about one third of the corresponding bending strength of a single coil pack from the toroidal magnet system operating in single mode. Table 9 lists performance parameters for the HDMS coil.

#### 4.5. Project status

The HDMS project is a three-year project that started in June 2018. The next project milestone is the combined critical design review and manufacturing readiness review taking place in December 2019.

Before building the HDMS coil, we will build a series of small solenoid test coils to compare different cable configurations and types of metal insulation. The cable configuration and metal insulation, that according to the test coil results, are most suitable for the spectrometer magnet, will be



**Figure 16.** The mechanical structure of the demonstrator coil. The insulation and cover plate are hidden for the upper layer. The shapes of the coil layers are machined into the magnet former. Cover plates hold the coil layers in place. The two coil layers are electrically connected with a braided copper connector going through an elongated hole in the magnet former.

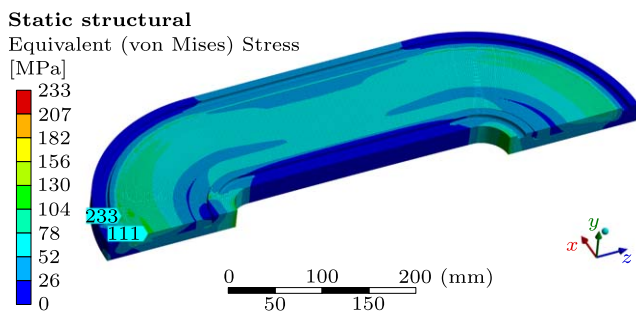


**Figure 17.** The equivalent (von Mises) stress on the demonstrator coil pack. Only one quarter of the coil pack is shown since the geometry is symmetric with respect to the  $xz$ -plane and  $yz$ -plane. The up-facing cover plate and insulation is hidden. The deformation is 14 times enhanced.

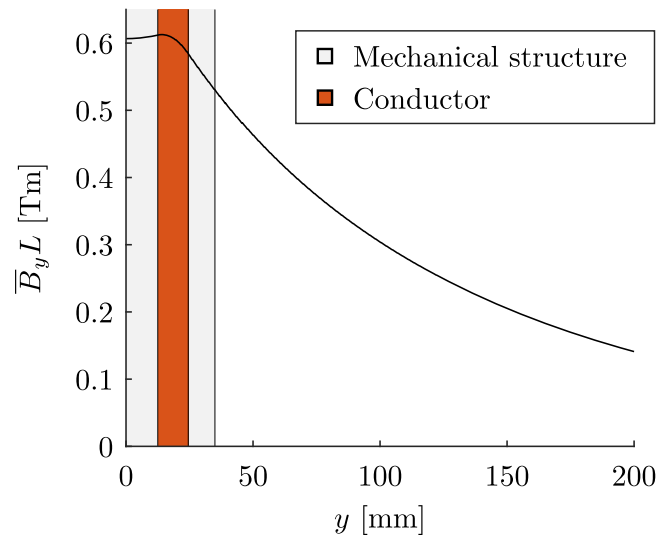


**Figure 19.** The bending strength as a function of  $y$  for the demonstrator coil.

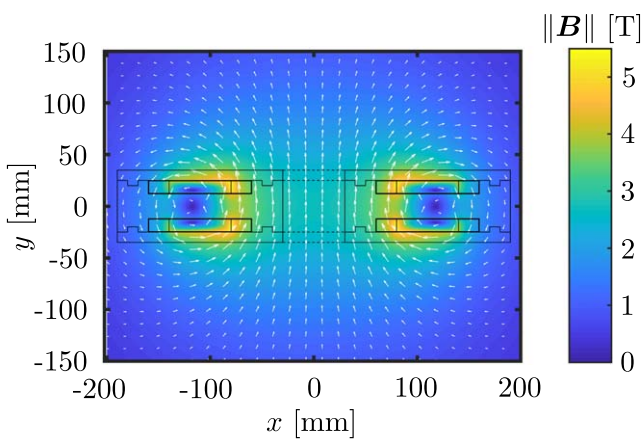


**Figure 18.** The boundaries of the coil and mechanical structure sketched on top of the magnetic field in the  $xy$ -plane for the demonstrator coil operating at  $J_{op} = 700 \text{ A mm}^{-2}$  at 4.2 K.

**Table 9.** Nominal performance parameters for the demonstrator coil.

Symbol	Description	Value	Unit
$B_{xy}$	Maximum $B$ -field in $xy$ -plane	5.5	T
$B_0$	Magnetic field at the center	2.7	T
$B_{str}$	Maximum $B$ -field at $x = d_{str}/2$	1.0	T
$\max_y \overline{B}_y L$	Maximum bending strength	0.61	T m

implemented in the designs of the full toroidal system and the HDMS coil. We plan to manufacture the HDMS coil in the first half of 2020 and test it in second half of 2020.

## 5. Conclusion

We have developed a conceptual design of an HTS magnet system for a magnetic spectrometer for a particle physics experiment in space. The magnet system consists of twelve racetrack-shaped two-layer coils in a toroidal configuration. The magnet provides an average bending strength of 3 T m for particles moving in the central cross sectional plane of the toroid. This should allow the magnetic spectrometer to detect particles with rigidities up to 100 TV. In operating mode at 20 K the magnet has a peak magnetic field of 11.9 T. Building the complete magnet system requires about 62 km of 12 mm wide HTS tape with an engineering critical current density of 1200 A mm<sup>-2</sup> at 4.2 K and 20 T. A short model demonstrator coil, called the HDMS coil, will be manufactured and tested. In operating mode at 4.2 K the HDMS coil has a peak magnetic field of 6.4 T. The HDMS coil requires 1 km of 12 mm wide HTS tape with an engineering critical current density of 400 A mm<sup>-2</sup> at 4.2 K and 20 T.

## ORCID iDs

Magnus Dam  <https://orcid.org/0000-0002-6707-9548>  
 Roberto Battiston  <https://orcid.org/0000-0002-5808-7239>  
 William Jerome Burger  <https://orcid.org/0000-0003-1977-6354>  
 Enrico Chesta  <https://orcid.org/0000-0002-9702-0627>  
 Roberto Iuppa  <https://orcid.org/0000-0001-5038-2762>  
 Gijs de Rijk  <https://orcid.org/0000-0002-8655-6995>  
 Lucio Rossi  <https://orcid.org/0000-0003-2158-7288>

## References

- [1] Rossi L, Sorbi M and Spillantini P 2004 *IEEE Trans. Appl. Supercond.* **14** 1696–9
- [2] Battiston R, Burger W J, Calvelli V, Datskov V I, Farinon S and Musenich R 2013 *IEEE Trans. Appl. Supercond.* **23** 4101604
- [3] Bruce R and Baudouy B 2015 *Phys. Proc.* **67** 264–9
- [4] Green M, Smoot G, Golden R, Israel M, Kephart R, Niemann R, Mewalt R, Ormes J, Spillantini P and Wiedenbeck M 1987 *IEEE Trans. Magn.* **23** 1240–3
- [5] Blau B, Harrison S M, Hofer H, Horvath I L, Milward S R, Ross J S H, Ting S C C, Ulbricht J and Viertel G 2002 *IEEE Trans. Appl. Supercond.* **12** 349–52
- [6] Battiston R 2019 *High Precision Particle Astrophysics as a New Window on the Universe with an Antimatter Large Acceptance Detector In Orbit (ALADInO) - A White Paper submitted in response to ESA's Call for the VOYAGE 2050 long-term plan* University of Trento
- [7] Aguilar M et al (AMS Collaboration) 2002 *Phys. Rep.* **366** 331–405
- [8] Blau B, Harrison S, Hofer H, Milward S, Kaiser G, Ross J S, Ting S and Ulbricht J 2004 *Nucl. Instrum. Methods Phys. Res.* **518** 139–42
- [9] Harrison S M, Ettliger E, Kaiser G, Blau B, Hofer H, Horvath I L, Ting S C C, Ulbricht J and Viertel G 2003 *IEEE Trans. Appl. Supercond.* **13** 1381–4
- [10] Lübelmeyer K et al 2011 *Nucl. Instrum. Meth. A* **654** 639–48
- [11] Battiston R and AMS-02 Collaboration 2008 *Nucl. Instrum. Meth.* **588** 227–34
- [12] Chang J et al (DAMPE Collaboration) 2017 *Astropart. Phys.* **95** 6–24
- [13] An Q (DAMPE Collaboration) et al 2019 *Sci. Adv.* **5** eaax3793
- [14] Chen H 2000 *Sci. China Ser. A* **43** 996–1008
- [15] Schael S et al 2019 *Nucl. Instrum. Methods Phys. Res. A* **944** 162561
- [16] Mager M and ALICE Collaboration 2016 *Nucl. Instrum. Methods Phys. Res. A* **824** 434–8
- [17] Rinella G A and ALICE Collaboration 2017 *Nucl. Instrum. Methods Phys. Res. A* **845** 583–7
- [18] Ricci E, Di Ruzza B, Iuppa R, Serra E, Manea C and Rashevskaya I 2019 *Il Nuovo Cimento C* **42** 209
- [19] Tanabashi M et al (Particle Data Group) 2018 *Phys. Rev. D* **98** 030001
- [20] ten Kate H H J and ATLAS Collaboration 2008 *Physica C* **468** 2137–42
- [21] Herve A and CMS Collaboration 2000 *IEEE Trans. Appl. Supercond.* **10** 389–94
- [22] Bianchi S and VEGA Integrated Project Team (IPT) 2008 *Acta Astronaut.* **63** 416–27
- [23] Dreyer L 2009 Latest developments on SpaceX's Falcon 1 and Falcon 9 launch vehicles and Dragon spacecraft 2009 *IEEE Aerospace Conf.* 1–15
- [24] Celani F 2015 *Acta Astronaut.* **107** 87–96
- [25] Duband L 2015 *Phys. Proc.* **67** 1–10
- [26] Battiston R 2011 Space Borne Experiments *Detectors for Particles and Radiation. Part 2: Systems and Applications (Landolt-Börnstein-Group I Elementary Particles, Nuclei and Atoms 21B2)* ed C W Fabjan and H Schopper (Berlin Heidelberg: Springer-Verlag) Part of Springer Materials ([https://doi.org/10.1007/978-3-642-14142-3\\_4](https://doi.org/10.1007/978-3-642-14142-3_4))
- [27] Allison J et al 2006 *IEEE Trans. Nucl. Sci.* **53** 270–8
- [28] Rossi L et al 2018 *IEEE Trans. Appl. Supercond.* **28** 1–10
- [29] Danial M and Van Nugteren J 2017 *Parameterization of the critical surface of REBCO conductors from Bruker CERN-STUDENTS-Note-2017-013* CERN
- [30] Hahn S, Park D K, Bascunan J and Iwasa Y 2011 *IEEE Trans. Appl. Supercond.* **21** 1592–5
- [31] Wang X, Hahn S, Kim Y, Bascuñán J, Voccio J, Lee H and Iwasa Y 2013 *Supercond. Sci. Technol.* **26** 035012
- [32] Hahn S, Kim K, Kim K, Lee H and Iwasa Y 2018 *TEION KOGAKU (J. Cryo. Super. Soc. Japan)* **53** 2–9
- [33] File J, Mills R G and Sheffield G V 1971 *IEEE Trans. Nucl. Sci.* **18** 277–82
- [34] Lequeu P, Smith K P and Daniélou A 2010 *J. Mater. Eng. Perform.* **19** 841–7
- [35] Allen N C, Chiesa L and Takayasu M 2015 *IOP Conf. Ser.: Mater. Sci. Eng.* **102** 012025
- [36] Sigmund O and Maute K 2013 *Struct. Multidiscipl. Optim.* **48** 1031–55